

# Volumetric density measurement in buoyant plumes using Tomographic Background Oriented Schlieren (TBOS)

Javed Mohd<sup>1</sup> and Debopam Das<sup>1,2\*</sup>

<sup>1</sup>Department of Aerospace Engineering, Indian Institute of Technology Kanpur, Kanpur, 208016, Uttar Pradesh, India.

<sup>2</sup>Department of Sustainable Energy Engineering, Indian Institute of Technology Kanpur, Kanpur, 208016, Uttar Pradesh, India.

\*Corresponding author(s). E-mail(s): [das@iitk.ac.in](mailto:das@iitk.ac.in);  
Contributing authors: [javedm@iitk.ac.in](mailto:javedm@iitk.ac.in);

## Abstract

Buoyant plumes are encountered in both natural and artificial scenarios, ranging from volcanic ash clouds and wildfires to smoke from chimneys and industrial pollutant discharge to rivers and lakes. These plumes are driven by the buoyancy forces arising from the density differences between the plume and the ambient fluids. Measurements of three dimensional density field is limited in literature and not available for buoyant plumes. Such data can lead to better understanding of the pollutant dispersion as well as fundamental nature of concentration dispersion in three-dimensional and turbulent flow. We present the three-dimensional density field measurement in buoyant plumes, particularly for forced and lazy plumes, using an in-house developed experimental rig and associated processing software. The density field reconstruction has been obtained using the tomographic background-oriented Schlieren (TBOS) technique. The experimental rig consists of eight cameras, facing random dot backgrounds placed diametrically opposite, mounted circumferentially around the buoyant plume. For the dot displacement calculation, we use a cross-correlation method. A finite difference-based Poisson solver is employed to calculate projected integrated density. The reconstruction has been performed using the Simultaneous Algebraic Reconstruction Technique (SART). The three-dimensional density field data, thus obtained is validated using existing theoretical models in the literature. We demonstrate that the 3D density field can serve as valuable data for validating and improving theoretical models of plume dynamics e.g. for the lazy plumes the measured density field is effectively used to show the puffing phenomenon.

**Keywords:** BOS, Tomo BOS, TBOS, buoyant plume, 3D density

## 1 Introduction

Many natural phenomena such as volcanic ash plumes ([Andrews and Gardner, 2009](#); [Bonadonna et al., 2015](#)), cloud thermals ([Turner, 1969](#)), earth's mantle plumes ([Koppers et al., 2021](#)), wild fire plumes ([Finney et al., 2015](#); [Kukkonen et al.,](#)

[2014](#); [Chung and Koseff, 2023](#)), hydrothermal vents at the bottom of ocean ([Lupton et al., 1985](#)), glacial ice water melts into the sea ([Hewitt, 2020](#)), and river discharging into the ocean ([Horner-Devine et al., 2015](#); [Rowland et al., 2009](#)) are driven by the buoyancy forces due to density difference between the ambient fluid and the plume

fluid (Woods, 2010). Similar fluid flows are also encountered in several human made scenarios such as in heating and ventilation (Linden et al., 1990; Shrinivas and Hunt, 2014; Richardson et al., 2024), smoke/steam stacks from industries (Slawson and Csanady, 1967; Raputa et al., 2023), waste-water discharge into the water bodies (Koh and Brooks, 1975; Washburn et al., 1992), and plumes generated in deep sea mining (Newland and Woods, 2024).

Accurate modelling of such phenomenon is necessary to control many of the catastrophic effects of these environmental events, related to natural disasters involving volcanoes, wild fires, and global warming. The plumes from the industrial sources must be discharged such that there impact on the nearby human population and ecology is minimized. However, as described below the theoretical models for the prediction of such phenomenon are still not very accurate and a continuous effort is being put to improve them. The accurate measurement of the 3D density field could play a pivotal role.

A theoretical model developed by Morton Taylor and Turner (MTT) (Morton et al., 1956) is widely used to predict the dynamics of such phenomena. They derived governing equations taking a top hat profile of vertical velocity and density and by apply the conservation laws obtained the similarity solutions. This initial model for the buoyancy driven flows was developed for the idealized point source and axisymmetric flows. Recently, Several attempts have been made to extend these models for real world scenarios from finite area source and non-businesque plumes (Hunt and Van den Bremer, 2011; Ciriello and Hunt, 2020) .

The theoretical modelling uses the assumption that the entrainment velocity is proportional to the local vertical velocity for the closure, and thus usage a universal entrainment constant. However, several studies report that the assumption is not correct and report a variable entrainment coefficient (Richardson and Hunt, 2022; Cenedese, 2024). Therefore, the existing literature lacks a consensus regarding the entrainment coefficient. The calculation of entrainment coefficient requires the parameters- velocity and density.

Often, these theoretical models needs to be validated against the ground truth data that must be obtained from the measurements as in case

of measuring entrainment. Hence, to improve the predictive capabilities of the existing theoretical models or to develop new models one need the accurate and detailed measurements of the plume parameters, including the full volumetric density field, for validation.

Most of the measurements related to the buoyant plumes have been performed using liquid-in-liquid systems. In comparison to the liquid based buoyant plume systems, the gaseous buoyant plumes received less attention in terms of experimental measurements. A summary of such experimental measurements, both in liquid based and gas-based systmes, is given in the table 1.

Although tomographic BOS has been used in previous studies to measure 3D density fields in buoyant jets, flames and plumes, as highlighted below, significant limitations remain. Nicolas et al. (2016) obtained density reconstruction in four convective flows: a candle flame, a hot jet generated by a heat gun, and two helicoidal flames obtained by rotation of a gas burner. (Nicolas et al., 2017), further measured various underexpanded jet flows issued into quiescent air. (Hu et al., 2023) obtained 3D density of single and dual laminar flames of  $CH_4$ /air mixture. Akamine et al. (2023) obtained 3D density of a candle flame kept near a wall using plane mirrors. Unterberger and Mohri (2022) measured the volumetric density of a Bunsen and co-flow burner using premixed  $CH_4$ /air mixture with their evolutionary TBOS. Liu et al. (2021) measured the density and temperature in a commercial Bunsen burner that produces an asymmetric butane-air premixed flame. Atcheson et al. (2008) measured density in a gas burner using 16 cameras. Amjad et al. (2020, 2023) in heated jet using 15 camera setup.

Despite these significant advances in experimental technique, the available measurement data on buoyant plumes remain predominantly point or two dimensional, often limited to symmetric flow conditions, both for liquid as well as gas based buoyancy driven flow systems. As a result, the current literature lacks a comprehensive three-dimensional density data for buoyant plumes.

In this paper, we aim to address the critical gap as discussed above, extending upon our previous work Mohd and Das (2022), where we presented the results of proof of concept stage. Here, we extend the analysis by refining the technique

**Table 1:** Summary of measurement techniques used in buoyant plume experiments.

Measurement Technique, quantities	Author(s)
Dye, Qualitative spread	Batchelor (1954); Morton et al. (1956), Kitamura and Sumita (2011), Kalita et al. (2024), Kaye and Hunt (2009), Papanicolaou and Stamoulis (2020)
Shadowgraphy/Schlieren, Density gradient	Rogers and Morris (2009) (also dye), Burrridge et al. (2016), Webb et al. (2023) (+thermocouple)
PIV, Velocity	Sutherland et al. (2021)
Scalar point measurements, Temperature, density	Yuana and Cox (1996) (thermocouple), Shabbir and George (1994) (hotwire), Mi et al. (2001) (hw), Rouse et al. (1952)
PIV + PLIF, Velocity and Species concentration	Parker et al. (2020), Paillat and Kaminski (2014), Talluru et al. (2021), Milton-McGurk et al. (2021), Wang and Law (2002), Ai et al. (2006), O’hern et al. (2005)

including the cubic spline sinogram interpolation, considering weights generated in the reconstruction circle only, and performing computation on a very dense grid using hamming window. To the best of our knowledge, this is the first study to report full three-dimensional (3D) density field measurements in buoyant plumes, specifically for forced and lazy plumes from finite area sources. We developed an in-house buoyant plume measurement rig based on the work of Bharadwaj and Das (2017, 2019) along with the MATLAB-based software suite capable of processing BOS images and tomographically reconstructing 3D density field.

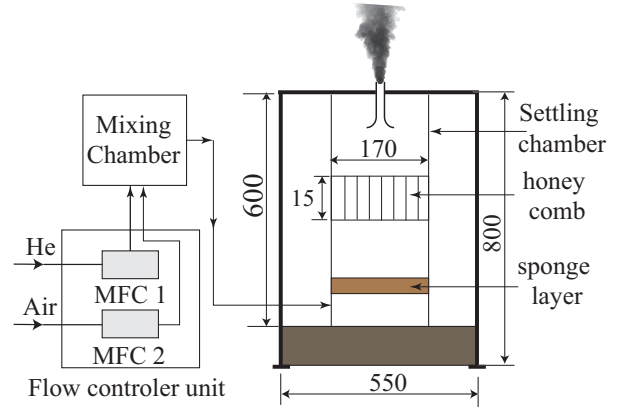
The remainder of this paper is organized as follows: Section 2 describes the methodology and experimental setup. In Section 3, we present and discuss the results, including validation of our novel measurements. Finally, conclusions and future directions are presented in Section 4.

## 2 Methodology

In this section we describe our experimental rig including the buoyant plume generation setup and Background-Oriented Schlieren (BOS) camera arrangements (2.1). Using this experimental rig, we obtain the raw images of the background with and without plume and process using our in-house software suit to obtain the volumetric density field. The work flow is described in section 2.2.

### 2.1 Buoyant plume generation and characterization

We describe the buoyant plume experimental rig in two parts, the apparatus used to generate a desired buoyant plume and the TBOS camera setup.

**Fig. 1:** Schematic of experimental setup for generating buoyant plumes.

The experimental setup for the generation of the buoyant plume is shown schematically in figure 1. Two mass flow controllers MFC 1 and MFC 2 (Alicat Scientific, MFC-100 slpm, MFC-1000 slpm) are used to precisely intake the dry helium (He) and air gases which are being supplied from the compressed gas cylinders. Inside a specially designed mixing chamber fitted with silencers

(Bharadwaj and Das, 2017), two gases are mixed, then fed to the vertically mounted settling chamber. Settling chamber has a sponge layer and honey-comb structure that helps to damp out any remaining flow disturbances and to straighten the flow. The He-Air mixture, finally pass through a bell shaped nozzle with exit diameter  $D = 35$  mm and discharges into the ambient air. The exit of the nozzle is fixed to a heavy steel bench platform. For further details of plume generation setup refer to (Bharadwaj and Das, 2017), however, the current setup does not include the seeding mechanism as the seeding is not required. The cuboid acrylic enclosure has also been removed for the ease of installing cameras and background patterns around the setup as described in figure 3. Experiments are performed in a quite room.

Given the flow rates  $Q_{\text{He}}$  (slpm) and  $Q_{\text{Air}}$  (slpm), taking the constant temperature and pressure during mixing, the equivalent source volume flow rate  $Q_0 = Q_{\text{He}} + Q_{\text{Air}}$ , and the equivalent mass flow rate  $m_0 = \rho_{\text{He}}Q_{\text{He}} + \rho_{\text{Air}}Q_{\text{Air}}$  are calculated. The reference properties of pure He and air gases taken for the analysis are presented in table 2. Further, the equivalent density of the mixture gas is given as  $\rho_0 = m_0/Q_0$ . The equivalent dynamic viscosity,  $\mu_0$  of the mixture is calculated using Wilke's formula (Wilke, 1950). The exit velocity at source,  $V_0 = Q_0^2/\pi b_0^2$ , where  $b_0 = D/2$  is the source radius. The buoyant plumes are characterized using the parameters in table 3.

**Table 2:** Properties of helium (He) and air used in the analysis

Property	He	Air
density ( $\rho$ ), kg/m <sup>3</sup>	0.1635	1.184
dynamic viscosity ( $\mu$ ), Pa-s	1.984e-5	1.849e-5
molecular weight ( $m_w$ ), g/mol	4.0026	28.966
Gladstone-Dale constant ( $G$ ) <sup>1</sup> , m <sup>3</sup> /kg	1.960e-04	2.239e-4

Experiments were conducted at 298 K temperature and 1 atm pressure.

<sup>1</sup>Data from Merzkirch (2012).

The parameters given in table 3 are the mass fractions  $Y$ , density ratio  $S = \rho_0/\rho_\infty$ , Reynolds number  $Re = \rho_0 V_0 D/\mu_0$ , Froud number  $Fr = V_0/\sqrt{gD}$ , and Richardson number  $Ri = (\rho_0 - \rho_\infty)gD/\rho_0 V_0^2$ . Where  $\rho_0$ ,  $\rho_\infty$ ,  $V_0$ , and  $D$  are the

density of source, density of ambient air, velocity at source and diameter at source respectively.

The Gladstone-Dale constant at source ( $G_0$ ) for the He-Air mixture Qin et al. (2002); Hu et al. (2024) is calculated as:

$$n = \rho(G_{\text{He}}Y_{\text{He}} + G_{\text{Air}}Y_{\text{Air}}) + 1 \quad (1)$$

$$n = \rho G + 1 \quad (2)$$

resulting in:

$$G = G_{\text{He}}Y_{\text{He}} + G_{\text{Air}}Y_{\text{Air}} \quad (3)$$

where  $Y_{\text{He}} = 1 - Y_{\text{Air}}$ ,  $G_{\text{He}}$  and  $G_{\text{Air}}$  are taken as in table 2. The value of  $G$  is assumed to be constant throughout the plume field and is taken equal to the source  $G_0$  value where the mass fractions-  $Y_{\text{He}}$  and  $Y_{\text{Air}}$  are known.

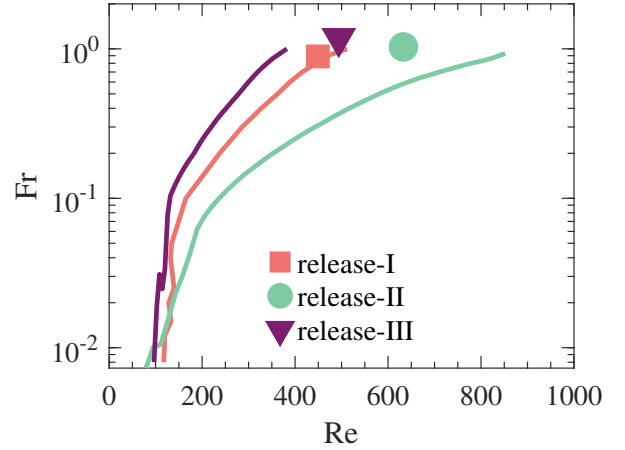


**Fig. 2:** Classifying three plume releases into laminar and puffing regimes using the neutral curves (solid lines) of the primary mode, based on the data of (Bharadwaj and Das, 2017).

Using the neutral curves for the stability of the buoyant plume with global stability analysis as given in (Bharadwaj and Das, 2017), we classify the three cases considered in the current study into one laminar (case-II) and two unstable, puffing, (case-I and III) (see fig. 2). This characteristic will be used in the results section to validate our measurements of volumetric density field.

Figure 3 depicts the schematic of camera arrangement for tomographic BOS measurement of the buoyant plume. Eight IMPERX B2320M cameras (2352 x 1768 px) with 85 mm lenses, each facing a background pattern are placed on a circle

**Table 3:** Characterization of the buoyant plumes at source (denoted by subscript ‘0’).

Release	$\dot{Q}$ (slpm)		$Y_{\text{He}}$	$Y_{\text{Air}}$	$\rho_0$	$\mu_0 (\times 10^{-5})$	$S_0$	$Re_0$	$Fr_0$	$Ri_0$	$G_0 (\times 10^{-4})$
	He	Air			$[\frac{kg}{m^3}]$	$[Pa \cdot s]$					$[\frac{m^3}{kg}]$
I	20	10	0.22	0.78	0.5037	2.04	0.43	449	0.89	1.72	2.1786
II	20	15	0.16	0.84	0.6009	2.01	0.51	633	1.03	0.91	2.1956
III	30	10	0.29	0.71	0.4186	2.06	0.35	494	1.18	1.31	2.1573

around the buoyant plume in such a way that the line-of-sight of the camera and background passes through the center of the measurement volume. The radius of the circle and angular spacing being 660 mm and  $22.5^\circ$ , respectively.

The cameras are rigidly mounted on heavy base stands. The camera and nozzle centres are aligned by STANLEY<sup>®</sup> CL90, the twin-beam self-leveling cross-line laser. Furthermore, final adjustment are done based on the blurred nozzle image on the camera frame, when cameras are focused on the background. The central pixel of the nozzle center is set at the half width of camera frame and the image edges are aligned perpendicular to the nozzle exit plane. This two-step alignment procedures ensures that the optical axis of each camera passes through the center of the nozzle. Distance of the each camera and nozzle is verified by noting down the width of the nozzle in each camera image. The angular position was also checked by pasting a protractor printed on paper around the nozzle and then aligning the camera optical axis such that the angle mark on the protractor aligns to the central pixel of the camera frame. The plane of the background pattern, lens plane and sensor plane all are parallel to each other. Hence, only a scaling factor is sufficient for calibration.

The background patterns are being illuminated with a stable high-power 40 W LED. All the eight cameras are synchronized using a hardware trigger signal obtained from *BNC Model 575 Digital/Delay Pulse Generator* at 10 fps with an exposure time of 100  $\mu s$  for acquiring the images simultaneously.

## 2.2 Data Processing work-flow

The raw images obtained from the bos experimental rig, with and without the presence of plumes (density gradient) are shown in figure 4. These images as obtained from each of the eight cameras

are subjected to further processing. The work flow pipeline for the processing is shown in figure 5.

### 2.2.1 Displacement vectors estimation

Given the two continuous image functions  $f(\alpha, \beta)$  and  $g(\alpha, \beta)$ , the continuous correlation function  $c(x, y)$  can be given as

$$c(x, y) = \int_{-\infty}^{\infty} \int_{-\infty}^{\infty} f(\alpha, \beta) g(\alpha + x, \beta + y) d\alpha d\beta \quad (4)$$

For the discretized images functions  $f(m, n)$  and  $g(m, n)$ , representing the background images with and without the density gradients of resolution  $M \times N$  pixels, the correlation can be calculated as

$$C(m', n') = \sum_{m=0}^{M-1} \sum_{n=0}^{N-1} f(m, n) \cdot g(m + m', n + n') \quad (5)$$

However, this approach is quite slow and generally a Fourier transform based approach ([Thielicke and Stamhuis, 2014](#); [Raffel et al., 2018](#)) using correlation theorem is used. The Fourier transform is faster since it usage the algorithm Fast Fourier Transform (FFT). According to correlation theorem

$$F[c(x, y)] = F[f(x, y)]F[g(x, y)], \quad (6)$$

where  $F[\cdot]$ , the two-dimensional Discrete Fourier Transform (DFT) of a discrete function  $f(m, n)$  over a grid of size  $M \times N$ , is given by:

$$F(k_x, k_y) = \sum_{m=0}^{M-1} \sum_{n=0}^{N-1} f(m, n) \exp \left\{ -2\pi i \left( \frac{k_x m}{M} + \frac{k_y n}{N} \right) \right\} \quad (7)$$



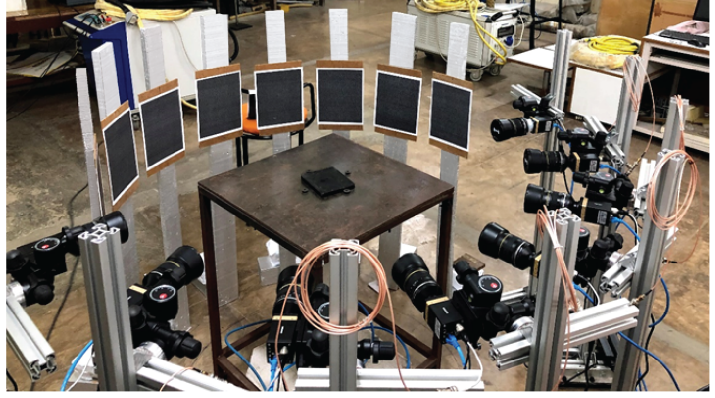
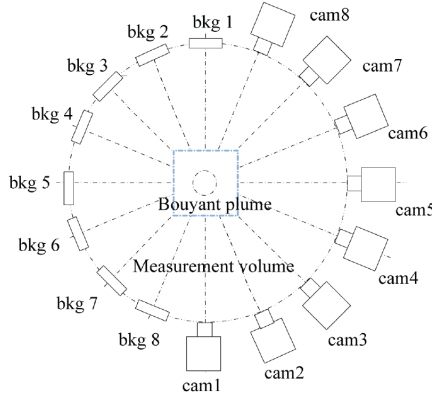


**Fig. 3:** 8-camera laboratory setup for Tomographic BOS, centred around the plume: (a) schematic and (b) actual experimental setup.

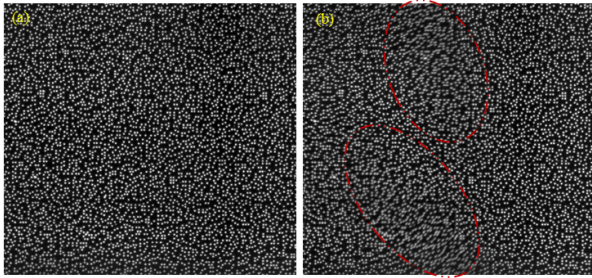


**Fig. 4:** Background images obtained from the experiment showing a cropped section of the full image: (a) without plume and (b) with plume.

where  $k_x \in \{0, 1, \dots, M-1\}$  and  $k_y \in \{0, 1, \dots, N-1\}$  are the frequency components in the  $x$ - and  $y$ -directions, respectively.

Therefore the correlation function

$$c(x, y) = F^{-1}[F[f(x, y)]F[g(x, y)]], \quad (8)$$

where  $F^{-1}[\cdot]$ , the two-dimensional Inverse Discrete Fourier Transform (IDFT), used to reconstruct the original function  $f(m, n)$  from its Fourier transform  $F(k_x, k_y)$ , is given by:

$$f(m, n) = \frac{1}{MN} \sum_{k_x=0}^{M-1} \sum_{k_y=0}^{N-1} F(k_x, k_y) \exp \left\{ 2\pi i \left( \frac{k_x m}{M} + \frac{k_y n}{N} \right) \right\} \quad (9)$$

where  $f(m, n)$  is reconstructed at each point  $(m, n)$  in the spatial domain.

Therefore, the cross-correlation function is calculated using Fourier transform of the two images, multiplying them and then taking inverse Fourier transform of the product. The background pattern images with and without density gradients have been processed using open source Matlab toolbox PIVlab (Thielicke and Stamhuis, 2014; Thielicke and Sonntag, 2021) using the FFT based multi pass cross-correlation (eqn. 8) as described above to obtain the cross correlation based displacements. The details of the processing are given in table 4.

**Table 4:** The details of the cross-correlation computation

Image Preprocessing	CLAHE 64 px Highpass filter 15 px weiner denoising 3px auto cont.
Analysis method	FFT window deformation
Inter. area (pass 1)	128 × 128 pixels (50% overlap)
Inter. area (pass 2)	64 × 64 pixels (50% overlap)
Inter. area (pass 2)	32 × 64 pixels (50% overlap)
Spurious vector filtering	velocity based validation
calibration	0.0773 mm/pixel

Figure 6 shows a representative displacement vector field obtained after processing the bos images from the figure 4 using the cross-correlation algorithm as described above. The vector displacements magnitude obtained from the computation, for all the eight cameras, at an arbitrary time instance, are shown in figure 7.

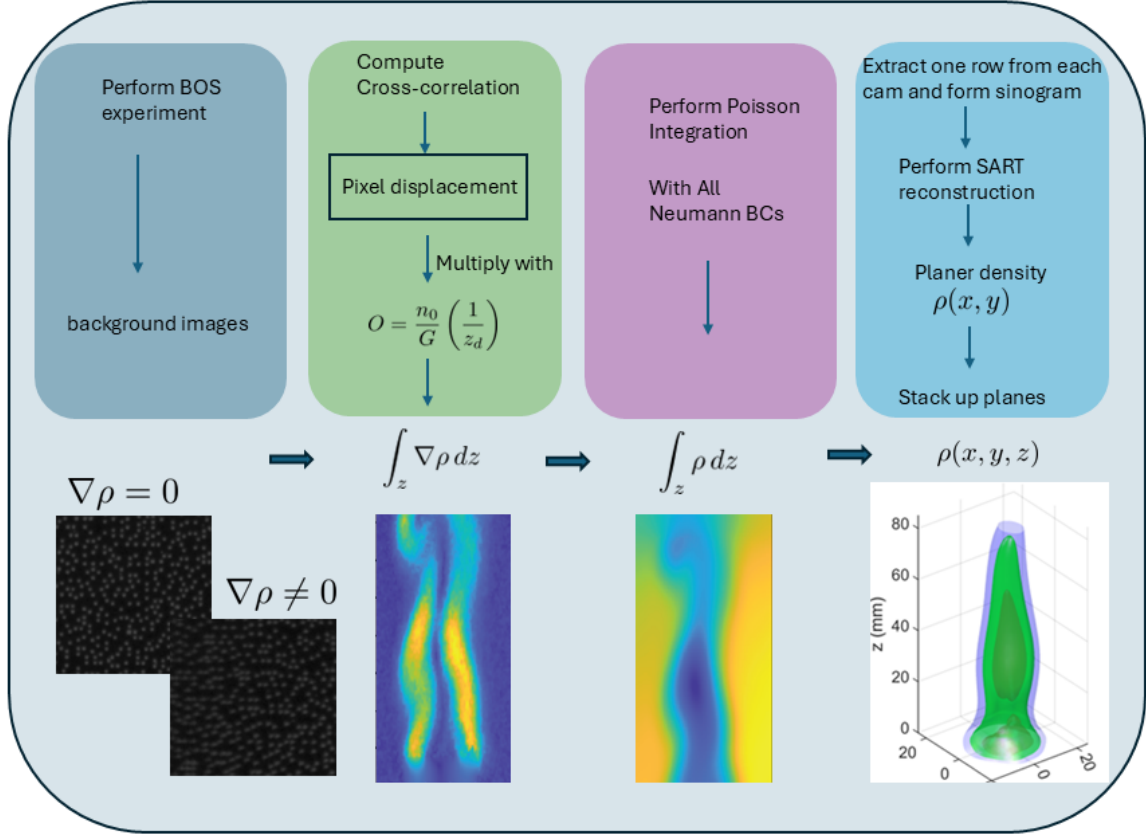


Fig. 5: Data processing chain of the developed TBOS system

### 2.2.2 Sinogram Interpolation

To increase the accuracy (Li et al., 2011) of the reconstruction from sparse angle tomographic measurements, the sinogram from sparse angle measurements (eight angles) is interpolated using cubic spline interpolation similar to Enjilela et al. (2019). The 2D discrete sinogram data has been interpolated using "interp2" function in Matlab, it incorporates the interpolation based on the cubic splines. After the interpolation the number of angular views increases from 8 to 15. A representative sinogram after the interpolation has been shown in figure 8.

### 2.2.3 Poisson solver for 3D density reconstruction

The projected density gradients ( $\int \nabla \rho dz$ ) given by the equation A3 using BOS are determined after implementing the cross-correlation on the background images with and without the plume. Our

goal in this step of the reconstruction work-flow is to obtain the projected density ( $\int \rho dz$ ) using the projected density gradients. To do that we formulate a Poisson problem to solve for projected density.

Consider the Poisson equation in 3D for a scalar-valued function  $\psi(x, y, z)$  as given by:

$$\nabla^2 \psi = \frac{\partial^2 \psi}{\partial x^2} + \frac{\partial^2 \psi}{\partial y^2} + \frac{\partial^2 \psi}{\partial z^2} = f(x, y, z), \quad (10)$$

where  $f(x, y, z)$  represents the source term. This equation can be discretized using finite difference method (FDM) on a 3D Cartesian grid with uniform grid spacing  $h_1$ ,  $h_2$ , and  $h_3$  in the  $x$ -,  $y$ -, and  $z$ -directions, respectively. For an interior grid point  $(i, j, k)$ , the second-order central differences in each spatial direction (7 point stencil with 3 points in each direction) yield the following discretized equation:

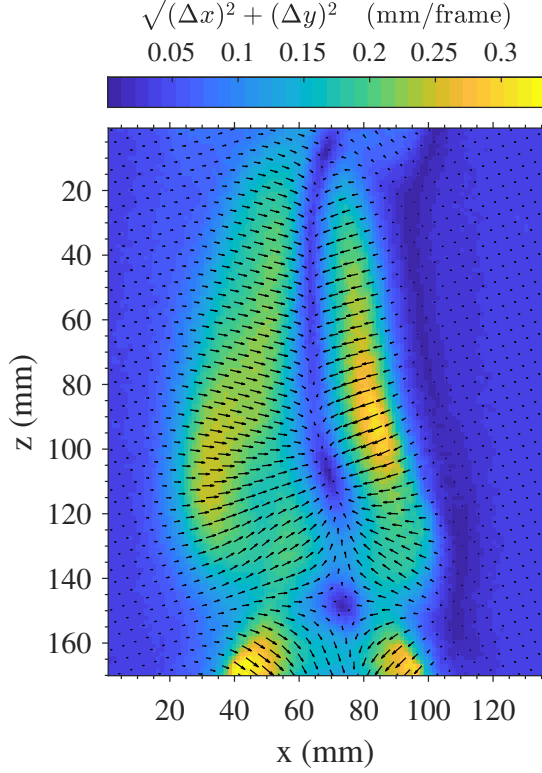


**Fig. 6:** Figure illustrating the displacement vectors obtained from the cross-correlation analysis of the background images with and without plume. The color represents the magnitude of vectors.

$$\frac{\psi_{i+1,j,k} - 2\psi_{i,j,k} + \psi_{i-1,j,k}}{h_1^2} + \frac{\psi_{i,j+1,k} - 2\psi_{i,j,k} + \psi_{i,j-1,k}}{h_2^2} + \frac{\psi_{i,j,k+1} - 2\psi_{i,j,k} + \psi_{i,j,k-1}}{h_3^2} = f_{i,j,k}. \quad (11)$$

The discretized equation when applied to each grid point (node) results in one equation. All the equations obtained from each node can be rearranged to form a linear system (equation 12). In the linear system, unknown  $\psi$  values are rearranged to form vector  $\underline{\psi}$  and the matrix  $A$  includes the coefficient of those unknown values. Therefore, equation 11 when applied to each internal node results in one row of the linear system,

$$A\underline{\psi} = \underline{f}, \quad (12)$$

where  $A$  is a sparse matrix and  $\underline{f}$  is the vector of source terms.

To formulate Poisson problem with projected density gradients, the source function  $f$ , defined in equation 10, is calculated as:

$$\mathbf{f} = \frac{\partial \Delta_x}{\partial x} + \frac{\partial \Delta_y}{\partial y} + \frac{\partial \Delta_z}{\partial z}, \quad (13)$$

where  $\Delta_x$  and  $\Delta_y$  are calculated using cross-correlation in PIVlab and the gradient in the optical direction is taken as  $\Delta_z = 0$ . We use Neumann boundary conditions  $\frac{\partial \psi}{\partial n} = 0$  on each face of our solution domain. Boundary conditions are incorporated into the system by appropriately modifying the matrix ( $A$ ) and the right-hand side vector ( $f$ ) of equation 12. The Dirichlet boundary condition  $\psi = \psi_0$  is used later on (section 2.2.4), post the reconstruction step, to correct for the remaining integration constant in the Poisson solution due to the use of all Neumann boundary conditions only.

We use MATLAB function '[L,U,P,Q,D] = lu(A)' to perform a sparse LU decomposition, which factorizes the matrix  $A$  as:

$$P(D \setminus A)Q = LU, \quad (14)$$

where  $L$  is a lower triangular matrix,  $U$  is an upper triangular matrix,  $P$  and  $Q$  are permutation matrices, and  $D$  is a diagonal scaling matrix that improves the stability and sparsity of the factorization.

The solution process is divided into two steps. Firstly, forward substitution is used to solve for an intermediate vector  $\mathbf{y}$  in the system  $L\mathbf{y} = P\mathbf{f}$ . Secondly, backward substitution is applied to solve for the final solution  $\mathbf{u}$  in the system  $U\mathbf{u} = \mathbf{y}$ . By utilizing row scaling via  $D$ , the factorization remains sparse and stable, allowing efficient computation for large-scale systems.

Note that the solution of the equation 12 represents the projected density fields,  $\int \rho dz$  for each of the 8 cameras. We further use these results from Poisson solver to reconstruct the  $\rho(x, y, z)$  using tomographic reconstruction algorithm as described in the following sections.



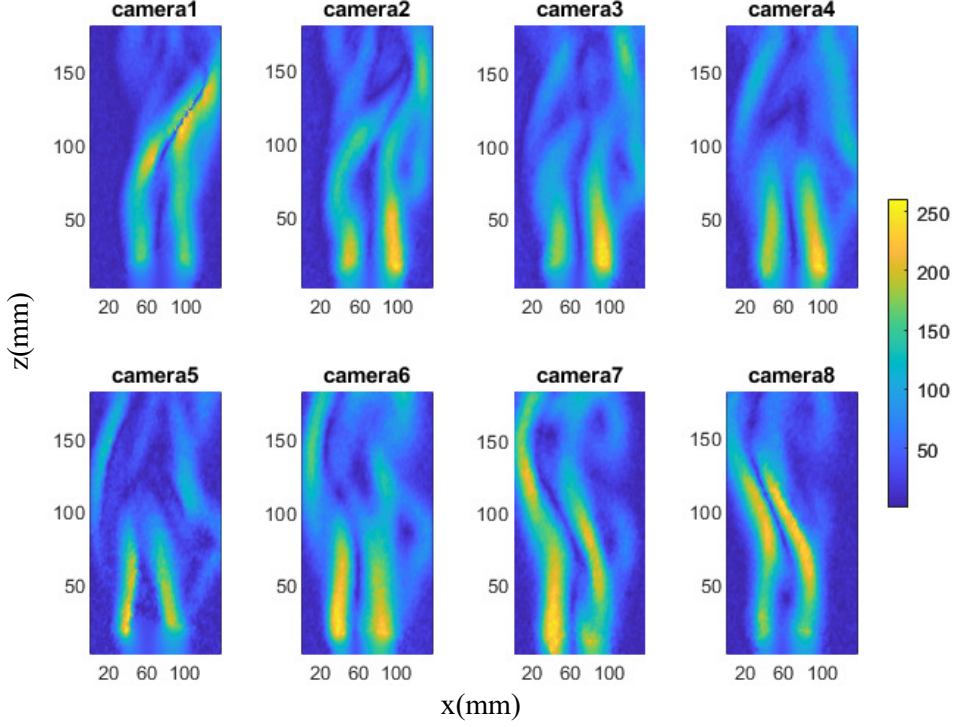


**Fig. 7:** Projected density gradient (represented by contour levels) from 8-cameras

#### 2.2.4 3D Reconstruction Process using SART

The forward projection model for the tomographic reconstruction process is first defined, followed by the methods used to solve the inverse problem. The projection is defined as the line integral of the function  $f(x,y)$  along the ray such as one at a perpendicular distance  $t$  from the origin and at an angle  $\theta$  (figure 10(a)). The ray can be uniquely defined by parameters-  $t$  and  $\theta$ . Also, noting that  $t = x\cos(\theta) + y\sin(90-\theta)$  for all the points on the ray, the projection for the ray  $(\theta, t)$  can be given as

$$p_\theta(t) = \int_{\text{line}(\theta,t)} f(x,y) ds$$

$$= \int \int_{\mathbb{R}^2} f(x,y) \delta(t - (x \cos \theta + y \sin \theta)) dx dy \quad (15)$$

$$= \mathcal{R}_i f(x,y) \quad (16)$$

where,  $\mathcal{R}$  denotes the Radon transform operator associated with the ray  $(\theta, t)$  denoted by ray index  $i$ . Assume, the function can be approximated by  $N$  basis functions  $\phi_j(x,y)$  as:

$$f(x,y) = \tilde{f}(x,y) = \sum_{j=1}^N f_j \phi_j(x,y) \quad (17)$$

where,  $f_j$  are the coefficients associated with the basis functions  $\phi_j(x,y)$ . Therefore, the equation 16, in terms of discretized function  $f(x,y)$  can be written as

$$p_i = \mathcal{R}_i \tilde{f}(x,y)$$

$$= \mathcal{R}_i \sum_{j=1}^N f_j \phi_j(x,y)$$

$$= \sum_{j=1}^N \{\mathcal{R}_i \phi_j(x,y)\} f_j$$

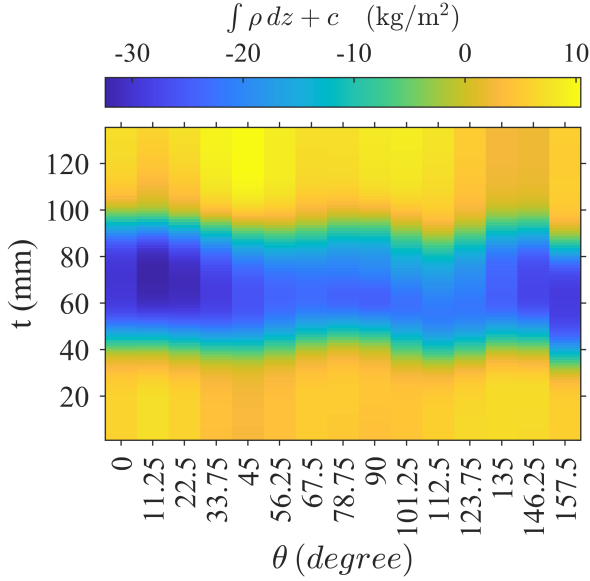


**Fig. 8:** A representative interpolated sinogram, showing the interpolated values between the original 8 angles.

$$= \sum_{j=1}^N a_{ij} f_j \quad (18)$$

where,  $a_{ij}$  denotes the scaler obtained by applying operator  $\mathcal{R}_i$  on  $j^{th}$  basis function  $\phi_j(x, y)$ .

The line integral for Radon transform can also be calculated by sum of discrete values of function  $\tilde{f}(s_{ip})$  at points  $1 < p < P$  at regular intervals  $\delta_p$  (figure 10(a)) on the ray inside the domain -

$$p_i = \sum_{p=1}^P \tilde{f}(s_{ip}) \delta_p \quad (19)$$

where, the values  $\tilde{f}(s_{ip})$  are calculated using the bilinear interpolation of the basis function surrounding the  $p^{th}$  point on  $i^{th}$  ray. For ease of forming linear system of equation, it is written as a bilinear contribution from all the shape functions (equation 20). However, only the four basis functions surrounding the point contribute, as the support of the pyramid-shaped basis functions is limited to the adjacent nodes (figure 10(b)).

$$\tilde{f}(s_{ip}) = \sum_{j=1}^N w_{ijp} f_j, \quad (20)$$

where  $w_{ijp}$  is the weight contribution from  $j^{th}$  basis function  $\phi_j$  to the  $p^{th}$  point on  $i^{th}$  ray (figure 10(a)).

Now, equation 19 can be written as

$$\begin{aligned} p_i &= \sum_{p=1}^P \sum_{j=1}^N w_{ijp} f_j \delta_p \\ &= \sum_{j=1}^N \left\{ \sum_{p=1}^P w_{ijp} \delta_p \right\} f_j \end{aligned} \quad (21)$$

Comparing eqn 18 and 21, the coefficients  $a_{ij}$  can be obtained as

$$a_{ij} = \sum_{p=1}^P w_{ijp} \delta_p \quad (22)$$

Therefore, the final linear system obtained by modelling forward projection can be given as

$$\mathcal{A} \vec{f} = \mathbf{p} \quad (23)$$

where  $(\mathcal{A})$  is the matrix,  $(\vec{f})$  is the vector of unknowns, and  $(\mathbf{p})$  is the projection vector obtained as the solution of eqn. 12. This inverse problem (eqn. 23) will be solved using kaczmarz methods of solving algebraic equations (Kaczmarz, 1937; Kak and Slaney, 2001).

In this study, the Simultaneous Algebraic Reconstruction Technique (SART), a variant of ART, is employed to develop an in-house code for reconstructing the instantaneous density field using data obtained from BOS measurements. Unlike ART, where the solution  $\vec{f}$  is updated after the consideration of each ray, SART averages the corrections for all the rays and uses the averaged value to update the solution. This completes one iteration, and the process continues until a suitable convergence criterion is met. The iteration step in SART can be mathematically represented as follows:

$$\vec{f}^{(k+1)} = \vec{f}^{(k)} + \frac{1}{M} \sum_{i=1}^M \left( \frac{p_i - \vec{a}_i \cdot \vec{f}^{(k)}}{\vec{a}_i \cdot \vec{a}_i} \right) \vec{t}_i, \quad (24)$$

where the vector of unknowns at  $k^{th}$  iteration is  $\vec{f}^{(k)} = [f_1, f_2, \dots, f_N]^T$ ,  $\vec{a}_i = [a_{i1}, a_{i2}, \dots, a_{iN}]$  represents the  $i^{th}$  row of the matrix  $\mathcal{A}$  with elements  $a_{ij}$ , and  $\vec{t}_i = [t_{i1}, t_{i2}, \dots, t_{iN}]$  is the  $i^{th}$  row of the matrix with elements  $t_{ij}$ .  $N$  is the total

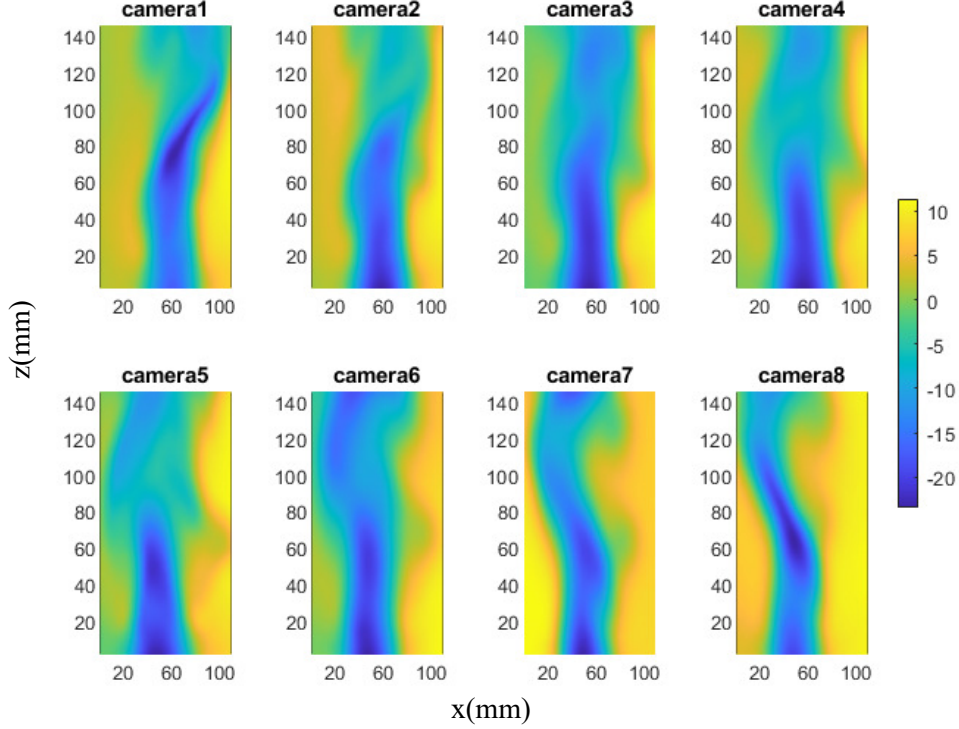


**Fig. 9:** Poisons integrated density field (represented by contour levels) from 8-cameras.

number of unknowns or grid points, and  $M$  is the total number of projection rays. The initial guess for the solution vector  $\bar{f}^{(0)}$  is set to zero.

The elements  $t_{ij}$  are calculated as:

$$t_{ij} = \sum_{p=1}^P h_{ip} w_{ijp} \delta_p, \quad (25)$$

where  $h_{ip}$ , for  $1 < p < P$ , is the Hanning window applied along the ray  $i$  over  $P$  discrete points. The hanning window along each projection ray, similar to Hamming window that was found to give superior results (Andersen and Kak, 1984; Kak and Slaney, 2001), has been employed.

After the reconstruction, the density field is post-processed to correct the undetermined integration constant due to the use of all Neumann boundary conditions in the Poisson integration step as described in section 2.2.3. Using all Neumann boundary conditions a smoother transition in the solution is obtained. A Dirichlet boundary condition with source density  $\rho_0$  for each case at the first reconstruction plane at the nozzle exit is

used to correct for the integration constant. A representative reconstructed density plane is shown in figure 11.

### 3 Results

#### 3.0.1 Validation using plume theory

The instantaneous 3D density field measured for all three releases (table 3) is temporally averaged and shown in figure 12. The left column of each case shows individual planes as reconstructed using our TBOS processing code. The middle column shows the density field after stacking all the planes together and then taking slices through the axis of the plume. The right column shows the iso-surfaces at selected values. Three iso-surfaces are drawn at the density values ( $\text{kg/m}^3$ ) of 0.72 (innermost), 0.8 (middle), and 0.87 (outermost). As can be seen, all the three cases show the lowest density fluid near the source region (represented by red color). The density of the fluid increases as we move radially outward and in the downstream direction due to entrainment of heavier ambient



**Table 5:** Gaussian fit parameters

Release	I ( $S_0 = 0.43$ , $Ri_0 = 1.72$ )				II ( $S_0 = 0.51$ , $Ri_0 = 0.91$ )				III ( $S_0 = 0.35$ , $Ri_0 = 1.31$ )			
$z/D$	0.18	0.79	1.41	2.03	0.18	0.79	1.41	2.03	0.18	0.79	1.41	2.03
$g'_c$	11.96	9.74	8.87	8.21	10.06	8.12	7.01	6.05	14.25	11.05	9.34	7.63
$b_{g'}$ (mm)	15.78	13.34	12.95	13.33	15.55	13.11	12.20	12.15	14.89	12.13	10.68	9.30

range  $z/D=0.18$  to  $z/D=0.203$ . For each profile  $g'_c$  decreases consistently moving in the downstream direction showing the increase in density due to entrainment of heavier ambient air. The values of  $b_{g'}$ , the radial scaling, also decreases in the downstream direction showing the narrowing gaussian spread due to decrease in  $g'$  corroborating the increase in density due to entrainment of ambient air.

From the fit results given in figure 14, It can be seen that the profiles collapse tightly on a Gaussian curve and hence are self-similar (George Jr et al., 1977; Turner, 1979; Hunt and Van den Bremer, 2011; Ezzamel et al., 2015; Parker et al., 2020; Talluru et al., 2021; Milton-McGurk et al., 2021; Richardson and Hunt, 2022; Pang et al., 2025).

### 3.0.2 Volume Visualization of Reconstructed Density field

Volumetric visualization of the instantaneous density fields can illustrate the plume dynamics and its axial, radial and azimuthal variations which differ substantially than the time averaged density field presented in Fig. 12. This approach contrasts with the conventional 2D Planer Laser Induced Florescence (PLIF) and integral optical visualization such as schlieren and shadowgraphy. If the instantaneous volumetric density field from the current work could be combined with the velocity field, the plume dynamics and its entrainment characteristics can be accurately captured. Such detailed measurements can help develop better analytical model for entrainment. Additionally, these measurements can also provide the dynamics of the turbulent non-turbulent interfaces of flow where buoyancy effects are present. In the present work, we illustrate the nature of the instantaneous density field for the three release cases described below.

Figure 15 shows a representative time instances, arbitrarily selected, where the iso-surface (the right column) of the minimum density

remains attached to the source. The two higher density iso-surfaces surrounding the low density iso-surface denote a gradual increase of density due to ambient fluid entrainment. Three points, marked as ‘a’, ‘b’, and ‘c’ on the iso-surface visualization, are examined in the transverse (left column) and longitudinal (middle column) density planes. For Slightly forced plume (release II, top row) the longitudinal density planes reveal a gradual density increase within the innermost iso-surface (region around points ‘a’ and ‘b’). The acceleration effect due to buoyancy that arises from the density difference is clearly visible from the iso-surface plot and the longitudinal variations. The transverse density slices at point ‘a’, ‘b’, and ‘c’ show the azimuthal density variation, with a gradual density increase in both radial and downstream directions. The release-II does not exhibit a separated Low Density Pocket (LDP) of source fluid, unlike the remaining two releases as described below. This confirms the absence of puffing as expected from Fig 2 and a sustained and gradual entrainment of ambient heavier fluid into the plume, in the downstream direction, is observed.

For the lazy plumes in release-I and release-III, the puffing phenomenon characterized by the periodic formation and downstream convection of large-scale toroidal vortex (Cetegen and Kasper, 1996; Bharadwaj and Das, 2017, 2019) is captured. As the toroidal vortex, forming near the source, moves downstream, it grows in size and pinches (Xia and Zhang, 2018) the plume fluid, inscribed by the toroidal vortex core, around the plume axis. The Low-Density fluid Pockets (LDP), generated by the plume, pinch-off and travel downstream. The representative instances with the detached LDP are shown in figures 15 middle row and bottom row for release-I and release-III, respectively.

The LDP is annotated for release-I, along with the three points- ‘a’, ‘b’, and ‘c’ to examine the density in the transverse and longitudinal planes.



The point ‘b’ is taken within the marked LDP and other two points- ‘a’ and ‘b’ are upstream and downstream of it, respectively. The density variation around the innermost iso-surface representing LDP can be seen in the longitudinal slices (middle column) too. The density of the plume fluid increases towards the neck upto point ‘a’ from the source, continue to exist low only in a thin region around the plume axis at point ‘a’, at this instant. The higher density at point ‘a’ can also be confirmed by the transverse plane at ‘a’ (left column). From point ‘a’ to point ‘b’ as we move within the marked LDP, a relatively low density fluid is encountered at point ‘b’. The density increase radially outwards within the LDP as seen in the transverse slice ‘b’. Moving further downstream from point ‘b’ to ‘c’, LDP shrinks and vanishes before point ‘c’. The variation of density along the plume axis from ‘b’ to ‘c’ as seen in the transverse slices show the rise in the density. The transverse slices also confirms the density field to increase radially outward which is expected due to heavier ambient air entraining into the plume.

The puffing phenomenon for release-III as shown in the bottom row of figure 15 is expected to be prominent than release-I. It can be seen that the maximum radius of LDP at point ‘b’ and the minimum radius of neck at point ‘a’ are significantly larger and smaller, respectively, in comparison to the release-I. However, for the ellipsoidal LDP region, the major diameter (aligned to the plume axis) has now shrunk with respect to the minor axis (aligned radially). The density within the ellipsoidal LDP region decreases towards the center as seen in both longitudinal and transverse density planes. In this release compare to the release-I, the density increases due to ambient air entrainment in the downstream direction with a steeper rate as seen in the longitudinal and transverse density slices.

It is to be noted from the instability equations (Bharadwaj and Das, 2017) that puffing depends on  $Re$ ,  $Fr$  and  $S$ . The dependency of  $Re$  is insignificant on puffing and it’s frequency. Thus, the  $Fr$  and  $S$  become the most important parameters and the puffing is governed by the density difference and gravity (Bharadwaj and Das, 2017). Hence, for the release III that has lower  $Ri$  (a combination of  $Fr$  and  $S$ ) compared to the release I shows higher degree of puffing as observed from the density measurements.

## 4 Conclusion

This paper presents the first volumetric density measurements for the buoyant plumes of He-Air mixture using Tomographic Background-Oriented Schlieren (TBOS). A MATLAB-based software module, developed in-house, is employed for data processing and tomographic reconstruction computations. Three cases of buoyant plumes - one forced and two lazy puffing plumes are taken as the test cases. The reduced density profiles extracted at different heights above the source are found to be scaling quite well assuming the Gaussian shape, thus validating our results. We further showed that the density measurements can be used to study the dynamics of the plumes by using iso-surfaces. We showed the presence of the motion of the density pocket during the puffing for the lazy plume cases which is absent for the marginally forced plume. The developed technique would be further used in future works to study the dynamics of the buoyant plumes.

**Acknowledgments.** The authors acknowledge the contributions of Kuchimanchi K. Bharadwaj and Karthik Murthy in developing the buoyant plume generation setup.

## Declarations

- Funding: The corresponding author acknowledges the Bhabha Atomic Research Centre (BARC), Department of Atomic Energy, Government of India, for their partial support in the development of the TBOS system.
- Conflict of interest: There are no competing interests to be disclosed
- Ethics approval and consent to participate: Not applicable
- Consent for publication
- Data availability
- Materials availability
- Code availability
- Author contribution: JM - Conducted experiments, developed the analysis software module, analyzed data, and wrote the first draft; DD - Concetualized the research, provided supervision and guidance, reviewed and revised the manuscript

## Appendix A BOS

When a light ray passes through the measurement domain having a variable refractive index  $n(x, y) = 1 + G\rho(x, y, z)$ , it refracts according to the local value of  $n$ . The parameters  $G$  and  $\rho(x, y, z)$  are the Gladstone-Dale constant and density gradients. A ray point on the background  $o_b$ , in the absence of any density gradient, is getting imaged on the center pixel of the image plane. Here, only central ray from a pencil of rays emanating from point  $o_b$  are shown.

With the variable density in the domain, the ray passing through it gets refracted and to the camera, it seems to be coming from point  $p'$  on the background. This apparent point  $p'$  gets imaged as point  $p$  on the image plane. The displacement from  $o_b$  to  $p'$  can be decomposed into Cartesian components-  $\Delta x'$   $\Delta y'$ . These displacement components are caused by the density gradient in the  $x$  and  $y$  directions-  $\partial\rho/\partial x$  and  $\partial\rho/\partial y$ , respectively. In the following paragraph, we develop the relation between the two using the  $y$  component, a similar relation for the  $x$ -component will be inferred.

Note that the deviation of the rays path, as they enter and leave the domain are assumed to be very small in comparison to the total path travelled by the ray from background to the image plane under the assumption of paraxial optics (Greivenkamp, 2004; Merzkirch, 2012). The distances in the schematic are exaggerated for the ease of visualization. In reality the radius of the circles denoted by  $C_i$  and  $C_e$  are infinitesimally small, making the two rays to enter and leave at the center of these circles and to remain straight inside the domain. For the validity of this assumption,  $\Delta z_d \ll z_i + z_b$ . A small deviation caused by density variations inside the domain results in an angular displacement  $\epsilon_y$  at the exit  $C_e$ . This small  $\epsilon_y$  leads to a detectable deflection on the imaging plane due to the long ray path.

For the refraction of ray, the simplified Euler-Lagrange equation results in:

$$\epsilon_y = \int_{z_d - \Delta z_d}^{z_d + \Delta z_d} \frac{\partial n}{\partial y} \left( = G \frac{\partial \rho}{\partial y} \right) dz, \quad (\text{A1})$$

where  $\partial n / \partial y = G \partial \rho / \partial y$  is obtained from Gladstone-Dale relation.

Also, from the point  $p'$  on the background, assuming a small value of  $\epsilon_y$ :

$$\tan(\epsilon_y) \approx \epsilon_y = \frac{\Delta y}{z_d} \quad (\text{A2})$$

Now using eqn. A1 and A2:

$$\int_{z_d - \Delta z_d}^{z_d + \Delta z_d} \frac{\partial \rho}{\partial y} dz = \frac{\Delta y'}{G z_d} \quad (\text{A3})$$

We use the above eqn A3 for our Matlab based software module, where  $\Delta y'$  are directly obtained by PIV computation using PIVlab with calibration using a linear ruler.

Using the similarity triangle for the geometry of imaging of  $p'$ , the displacement in the vertical direction on the background  $\Delta y'$  and on the image plane  $\Delta y$  can be related as:

$$\frac{\Delta y}{z_i} = \frac{\Delta y'}{z_b} \quad (\text{A4})$$

Substituting  $\Delta y'$  in eqn. A3 by  $\Delta y$  from A4 results in:

$$\int_{z_d - \Delta z_d}^{z_d + \Delta z_d} \frac{\partial \rho}{\partial y} dz = \frac{1}{G z_d} \left( \frac{z_b}{z_i} \Delta y \right) \quad (\text{A5})$$

The eqn A5 (Merzkirch, 1987; Raffel et al., 2000; Richard and Raffel, 2001; Meier, 2002; Venkatakrishnan and Meier, 2004; Raffel, 2015), explicitly includes the camera parameters. The parameter  $z_i$  can be replaced by the focal length  $f$  using the thin lens formula  $1/z_b + 1/z_i = 1/f$ ; since  $z_b \gg z_i$ ,  $1/z_i = 1/f$ .

Using eqn. A5, the sensitivity (for a given density gradient, what would be the deflection on the image plane) can be given as:

$$\frac{\Delta y}{\nabla \rho} = G \frac{z_d}{z_b} f \quad (\text{A6})$$

The minimum deflection of the ray that can be detected by a camera system is one pixel. Therefore, the minimum measurable density gradient is:

$$\nabla \rho|_{\min} = \frac{1}{G} \frac{z_b}{z_d} \frac{\Delta_s}{f}, \quad (\text{A7})$$

where,  $\Delta_s$  being the pixel size in meters.

## References

- Andrews, B.J., Gardner, J.E.: Turbulent dynamics of the 18 may 1980 mount st. helens eruption column. *Geology* **37**(10), 895–898 (2009)
- Atcheson, B., Ihrke, I., Heidrich, W., Tevs, A., Bradley, D., Magnor, M., Seidel, H.-P.: Time-resolved 3d capture of non-stationary gas flows. *ACM transactions on graphics (TOG)* **27**(5), 1–9 (2008)
- Andersen, A.H., Kak, A.C.: Simultaneous algebraic reconstruction technique (sart): a superior implementation of the art algorithm. *Ultrasonic imaging* **6**(1), 81–94 (1984)
- Amjad, S., Karami, S., Soria, J., Atkinson, C.: Assessment of three-dimensional density measurements from tomographic background-oriented schlieren (bos). *Measurement Science and Technology* **31**(11), 114002 (2020)
- Ai, J., Law, A.W.-K., Yu, S.: On boussinesq and non-boussinesq starting forced plumes. *Journal of Fluid Mechanics* **558**, 357–386 (2006)
- Amjad, S., Soria, J., Atkinson, C.: Three-dimensional density measurements of a heated jet using laser-speckle tomographic background-oriented schlieren. *Experimental Thermal and Fluid Science* **142**, 110819 (2023)
- Akamine, M., Teramoto, S., Okamoto, K.: Formulation and demonstrations of three-dimensional background-oriented schlieren using a mirror for near-wall density measurements. *Experiments in Fluids* **64**(7), 134 (2023)
- Batchelor, G.: Heat convection and buoyancy effects in fluids. *Quarterly journal of the royal meteorological society* **80**(345), 339–358 (1954)
- Bharadwaj, K.K., Das, D.: Global instability analysis and experiments on buoyant plumes. *Journal of Fluid Mechanics* **832**, 97–145 (2017) <https://doi.org/10.1017/jfm.2017.665>
- Bharadwaj, K.K., Das, D.: Puffing in planar buoyant plumes: Biglobal instability analysis and experiments. *Journal of Fluid Mechanics* **863**, 817–849 (2019)
- Bonadonna, C., Pistolesi, M., Cioni, R., Degruyter, W., Elissondo, M., Baumann, V.: Dynamics of wind-affected volcanic plumes: The example of the 2011 cordón caulle eruption, chile. *Journal of Geophysical Research: Solid Earth* **120**(4), 2242–2261 (2015)
- Burridge, H., Partridge, J., Linden, P.: The fluxes and behaviour of plumes inferred from measurements of coherent structures within images of the bulk flow. *Atmosphere-Ocean* **54**(4), 403–417 (2016)
- Cenedese, C.: The entrainment hypothesis—80 years old and still going strong. *Journal of Fluid Mechanics* **1000**, 2 (2024)
- Ciriello, F., Hunt, G.: Analytical solutions and virtual origin corrections for forced, pure and lazy turbulent plumes based on a universal entrainment function. *Journal of Fluid Mechanics* **893**, 12 (2020)
- Cetegen, B.M., Kasper, K.D.: Experiments on the oscillatory behavior of buoyant plumes of helium and helium-air mixtures. *Physics of fluids* **8**(11), 2974–2984 (1996)
- Chung, H., Koseff, J.R.: Interaction of a buoyant plume with a turbulent canopy mixing layer. *Physical Review Fluids* **8**(6), 064501 (2023)
- Enjilela, E., Lee, T.-Y., Wisenberg, G., Teefy, P., Bagur, R., Islam, A., Hsieh, J., So, A.: Cubic-spline interpolation for sparse-view ct image reconstruction with filtered backprojection in dynamic myocardial perfusion imaging. *Tomography* **5**(3), 300 (2019)
- Ezzamel, A., Salizzoni, P., Hunt, G.R.: Dynamical variability of axisymmetric buoyant plumes. *Journal of Fluid Mechanics* **765**, 576–611 (2015)
- Finney, M.A., Cohen, J.D., Forthofer, J.M., McAllister, S.S., Gollner, M.J., Gorham, D.J., Saito, K., Akafuah, N.K., Adam, B.A., English, J.D.: Role of buoyant flame dynamics in wildfire spread. *Proceedings of the National Academy of Sciences* **112**(32), 9833–9838 (2015)
- George Jr, W.K., Alpert, R.L., Tamanini, F.:

- Turbulence measurements in an axisymmetric buoyant plume. *International Journal of Heat and Mass Transfer* **20**(11), 1145–1154 (1977)
- Greivenkamp, J.E.: Field guide to geometrical optics. (2004). SPIE Bellingham
- Horner-Devine, A.R., Hetland, R.D., MacDonald, D.G.: Mixing and transport in coastal river plumes. *Annual Review of Fluid Mechanics* **47**(1), 569–594 (2015)
- Hewitt, I.J.: Subglacial plumes. *Annual Review of Fluid Mechanics* **52**(1), 145–169 (2020)
- Hunt, G., Bremer, T.: Classical plume theory: 1937–2010 and beyond. *IMA journal of applied mathematics* **76**(3), 424–448 (2011)
- Hu, W., Yang, L., Zhang, Y., Wang, P., Li, J.: Reconstruction refinement of hybrid background-oriented schlieren tomography. *Physics of Fluids* **36**(2) (2024)
- Hu, W., Zhang, Y., Liang, X., Li, J., Yang, L.: Background-oriented schlieren measurements for asymmetrical laminar flames along arbitrary rays from a single view. *Experiments in Fluids* **64**(8), 145 (2023)
- Inc., T.M.: Evaluating Goodness of Fit. (2025). Accessed: 2025-01-25. <https://in.mathworks.com/help/curvefit/evaluating-goodness-of-fit.html>
- Kaczmarz, S.: Angenäherte auflösung von systemen linearer gleichungen. *Bulletin International de l'Académie Polonaise des Sciences et des Lettres A*, 355–357 (1937)
- Koh, R.C., Brooks, N.H.: Fluid mechanics of waste-water disposal in the ocean. *Annual Review of Fluid Mechanics* **7**(1), 187–211 (1975)
- Koppers, A.A., Becker, T.W., Jackson, M.G., Konrad, K., Müller, R.D., Romanowicz, B., Steinberger, B., Whittaker, J.M.: Mantle plumes and their role in earth processes. *Nature Reviews Earth & Environment* **2**(6), 382–401 (2021)
- Kalita, B., Florez, L.P., Landau, E., Ward, R., Holyoke, J., Johnson, B.A.: Characterizing visual structures in a buoyant plume. *Experiments in Fluids* **65**(9), 136 (2024)
- Kaye, N., Hunt, G.: An experimental study of large area source turbulent plumes. *International Journal of Heat and Fluid Flow* **30**(6), 1099–1105 (2009)
- Kukkonen, J., Nikmo, J., Sofiev, M., Riikonen, K., Petäjä, T., Virkkula, A., Levula, J., Schobesberger, S., Webber, D.: Applicability of an integrated plume rise model for the dispersion from wild-land fires. *Geoscientific Model Development* **7**(6), 2663–2681 (2014)
- Kak, A.C., Slaney, M.: Principles of Computerized Tomographic Imaging. SIAM, ??? (2001)
- Kitamura, S., Sumita, I.: Experiments on a turbulent plume: Shape analyses. *Journal of Geophysical Research: Solid Earth* **116**(B3) (2011)
- Li, Y., Chen, Y., Hu, Y., Oukili, A., Luo, L., Chen, W., Toumoulin, C.: Strategy of computed tomography sinogram inpainting based on sinusoid-like curve decomposition and eigenvector-guided interpolation. *Journal of the Optical Society of America A* **29**(1), 153–163 (2011)
- Lupton, J., Delaney, J., Johnson, H., Tivey, M.: Entrainment and vertical transport of deep-ocean water by buoyant hydrothermal plumes. *Nature* **316**(6029), 621–623 (1985)
- Liu, H., Huang, J., Li, L., Cai, W.: Volumetric imaging of flame refractive index, density, and temperature using background-oriented schlieren tomography. *Science China Technological Sciences* **64**(1), 98–110 (2021)
- Linden, P., Lane-Serff, G., Smeed, D.: Emptying filling boxes: the fluid mechanics of natural ventilation. *Journal of Fluid Mechanics* **212**, 309–335 (1990)
- Mohd, J., Das, D.: Development of tomographic background-oriented schlieren technique for 3d density measurement in buoyant plumes. In: *Conference on Fluid Mechanics and Fluid*

- Power, pp. 35–42 (2022). Springer
- Meier, G.: Computerized background-oriented schlieren. *Experiments in fluids* **33**(1), 181–187 (2002)
- Merzkirch, W.: *Flow visualization* 2nd edn (new york: Academic) (1987)
- Merzkirch, W.: *Flow Visualization*. Elsevier, ??? (2012)
- Milton-McGurk, L., Williamson, N., Armfield, S., Kirkpatrick, M., Talluru, K.: Entrainment and structure of negatively buoyant jets. *Journal of Fluid Mechanics* **911**, 21 (2021)
- Mi, J., Nobes, D., Nathan, G.: Influence of jet exit conditions on the passive scalar field of an axisymmetric free jet. *Journal of Fluid Mechanics* **432**, 91–125 (2001)
- Morton, B.R., Taylor, G.I., Turner, J.S.: Turbulent gravitational convection from maintained and instantaneous sources. *Proceedings of the Royal Society of London. Series A. Mathematical and Physical Sciences* **234**(1196), 1–23 (1956)
- Nicolas, F., Donjat, D., Léon, O., Le Besnerais, G., Champagnat, F., Micheli, F.: 3d reconstruction of a compressible flow by synchronized multi-camera bos. *Experiments in fluids* **58**, 1–15 (2017)
- Nicolas, F., Todoroff, V., Plyer, A., Le Besnerais, G., Donjat, D., Micheli, F., Champagnat, F., Cornic, P., Le Sant, Y.: A direct approach for instantaneous 3d density field reconstruction from background-oriented schlieren (bos) measurements. *Experiments in fluids* **57**, 1–21 (2016)
- Newland, E., Woods, A.: The dynamics of impinging plumes from a moving source. *Journal of Fluid Mechanics* **982**, 6 (2024)
- O’hern, T., Weckman, E., Gerhart, A., Tieszen, S., Schefer, R.: Experimental study of a turbulent buoyant helium plume. *Journal of Fluid Mechanics* **544**, 143–171 (2005)
- Parker, D., Burridge, H.C., Partridge, J., Linden, P.: A comparison of entrainment in turbulent line plumes adjacent to and distant from a vertical wall. *Journal of Fluid Mechanics* **882**, 4 (2020)
- Pang, M., Chauhan, K., Talluru, K.: Measurements of buoyant plumes in a turbulent boundary layer. *Experiments in Fluids* **66**(1), 1–13 (2025)
- Paillat, S., Kaminski, E.: Entrainment in plane turbulent pure plumes. *Journal of Fluid Mechanics* **755**, 2 (2014)
- Papanicolaou, P.N., Stamoulis, G.C.: Vertical round buoyant jets and fountains in a linearly, density-stratified fluid. *Fluids* **5**(4), 232 (2020)
- Qin, X., Xiao, X., Puri, I.K., Aggarwal, S.K.: Effect of varying composition on temperature reconstructions obtained from refractive index measurements in flames. *Combustion and Flame* **128**(1-2), 121–132 (2002)
- Raffel, M.: Background-oriented schlieren (bos) techniques. *Experiments in Fluids* **56**, 1–17 (2015)
- Richardson, J., Hunt, G.R.: What is the entrainment coefficient of a pure turbulent line plume? *Journal of Fluid Mechanics* **934**, 11 (2022)
- Raputa, V., Lezhenin, A., Amikishieva, R.: Estimates of the height of rise and buoyancy of smoke plumes from high chimneys of thermal power plants from satellite information. *Atmospheric and Oceanic Optics* **36**(6), 785–789 (2023)
- Rogers, M.C., Morris, S.W.: Natural versus forced convection in laminar starting plumes. *Physics of Fluids* **21**(8) (2009)
- Richard, H., Raffel, M.: Principle and applications of the background oriented schlieren (bos) method. *Measurement science and technology* **12**(9), 1576 (2001)
- Richardson, J., Radomski, S., Hunt, G.R.: Flow regimes in emptying–filling boxes with two



- buoyancy sources of differing strengths and elevations. *Journal of Fluid Mechanics* **988**, 12 (2024)
- Raffel, M., Richard, H., Meier, G.: On the applicability of background oriented optical tomography for large scale aerodynamic investigations. *Experiments in Fluids* **28**(5), 477–481 (2000)
- Rowland, J.C., Stacey, M.T., Dietrich, W.E.: Turbulent characteristics of a shallow wall-bounded plane jet: experimental implications for river mouth hydrodynamics. *Journal of Fluid Mechanics* **627**, 423–449 (2009)
- Raffel, M., Willert, C.E., Scarano, F., Kähler, C.J., Wereley, S.T., Kompenhans, J.: *Particle Image Velocimetry: a Practical Guide*. Springer, ??? (2018)
- Rouse, H., Yih, C., Humphreys, H.: Gravitational convection from a boundary source. *Tellus* **4**(3), 201–210 (1952)
- Slawson, P., Csanady, G.: On the mean path of buoyant, bent-over chimney plumes. *Journal of Fluid Mechanics* **28**(2), 311–322 (1967)
- Shabbir, A., George, W.K.: Experiments on a round turbulent buoyant plume. *Journal of Fluid Mechanics* **275**, 1–32 (1994)
- Shrinivas, A.B., Hunt, G.R.: Transient ventilation dynamics induced by heat sources of unequal strength. *Journal of fluid mechanics* **738**, 34–64 (2014)
- Sutherland, B., Ma, Y., Flynn, M., Frank, D., Linden, P., Lemasquerier, D., Le Bars, M., Pacary, C., Jamin, T., Dauxois, T., *et al.*: Plumes in rotating fluid and their transformation into tornados. *Journal of Fluid Mechanics* **924**, 15 (2021)
- Talluru, K.M., Armfield, S., Williamson, N., Kirkpatrick, M., Milton-McGurk, L.: Turbulence structure of neutral and negatively buoyant jets. *Journal of Fluid Mechanics* **909**, 14 (2021)
- Thielicke, W., Stamhuis, E.: Pivlab—towards user-friendly, affordable and accurate digital particle image velocimetry in matlab. *Journal of open research software* **2**(1) (2014)
- Thielicke, W., Sonntag, R.: Particle image velocimetry for matlab: Accuracy and enhanced algorithms in pivlab. *Journal of Open Research Software* **9**(1) (2021)
- Turner, J.: Buoyant plumes and thermals. *Annual Review of Fluid Mechanics* **1**(1), 29–44 (1969)
- Turner, J.S.: *Buoyancy Effects in Fluids*. Cambridge university press, ??? (1979)
- Unterberger, A., Mohri, K.: Evolutionary background-oriented schlieren tomography with self-adaptive parameter heuristics. *Optics Express* **30**(6), 8592–8614 (2022)
- Venkatkrishnan, L., Meier, G.: Density measurements using the background oriented schlieren technique. *Experiments in Fluids* **37**, 237–247 (2004)
- Wilke, C.R.: A viscosity equation for gas mixtures. *The journal of chemical physics* **18**(4), 517–519 (1950)
- Washburn, L., Jones, B.H., Bratkovich, A., Dickey, T., Chen, M.-S.: Mixing, dispersion, and resuspension in vicinity of ocean wastewater plume. *Journal of Hydraulic Engineering* **118**(1), 38–58 (1992)
- Wang, H., Law, A.W.-k.: Second-order integral model for a round turbulent buoyant jet. *Journal of Fluid Mechanics* **459**, 397–428 (2002)
- Woods, A.W.: Turbulent plumes in nature. *Annual Review of Fluid Mechanics* **42**(1), 391–412 (2010)
- Webb, J.P., Wise, N.H., Hunt, G.R.: Turbulent plumes above a heated plate. *Journal of Fluid Mechanics* **959**, 29 (2023)
- Xia, X., Zhang, P.: A vortex-dynamical scaling theory for flickering buoyant diffusion flames. *Journal of Fluid Mechanics* **855**, 1156–1169 (2018)
- Yuana, L.-M., Cox, G.: An experimental study of some line fires. *Fire Safety Journal* **27**(2), 123–139 (1996)

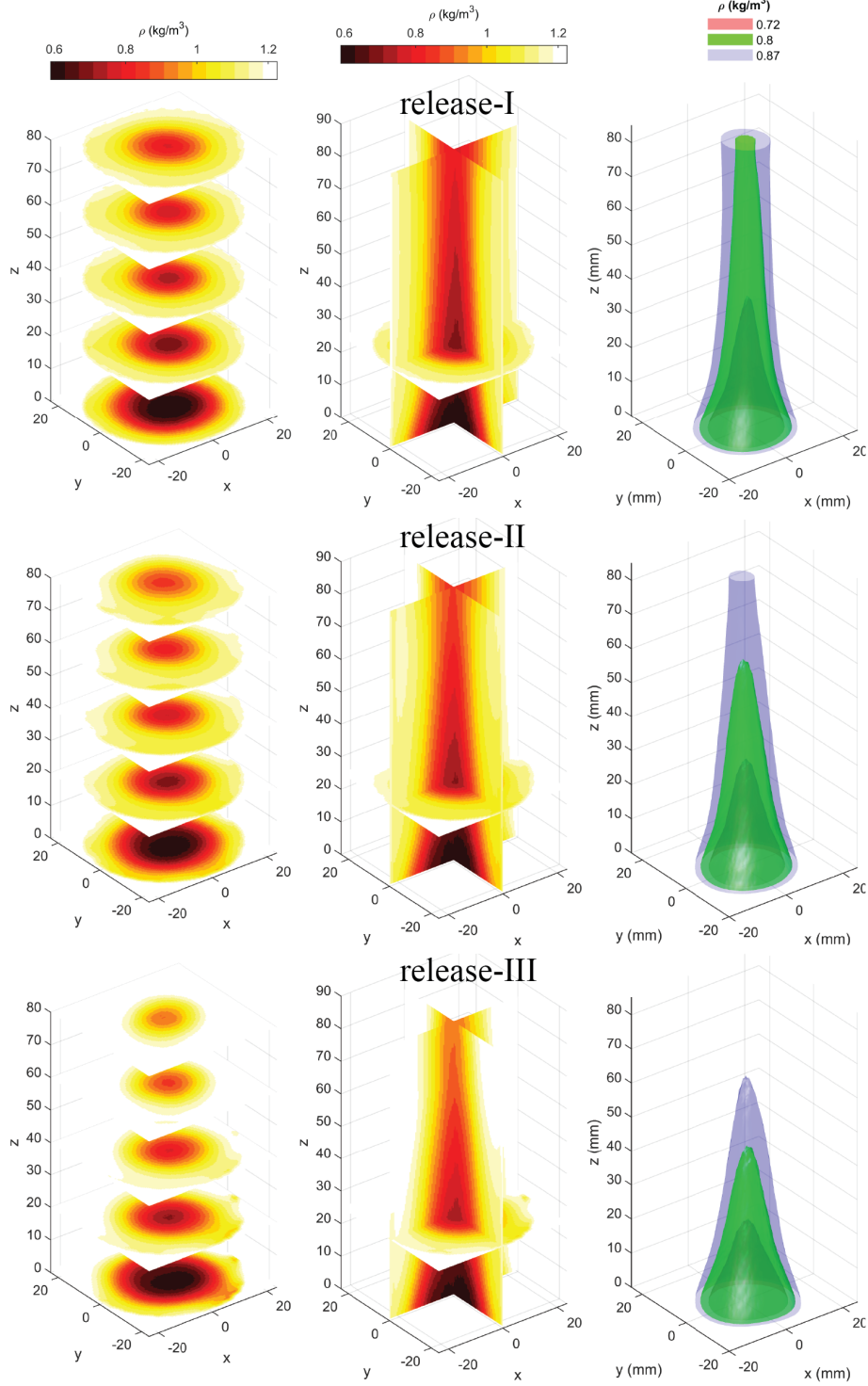


**Fig. 12:** Volume visualization of time-averaged density for all three releases: I (top row), II (middle row), and III (bottom row). The right column shows iso-surface visualizations, the middle column features longitudinal density planes that highlight internal variations within the iso-surfaces, and the left column presents transverse density slices to capture radial variations.

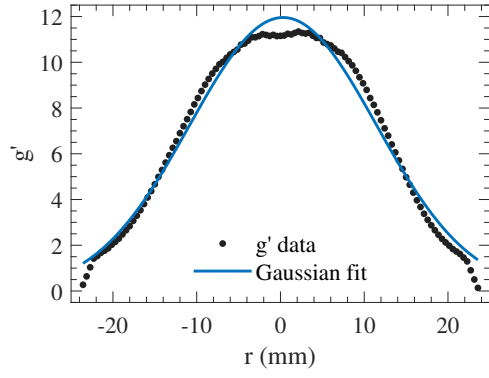


**Fig. 13:** Representative figure showing the Gaussian curve fit to the  $g'$  profile extracted at  $z/D = 0.18$  for release-I.

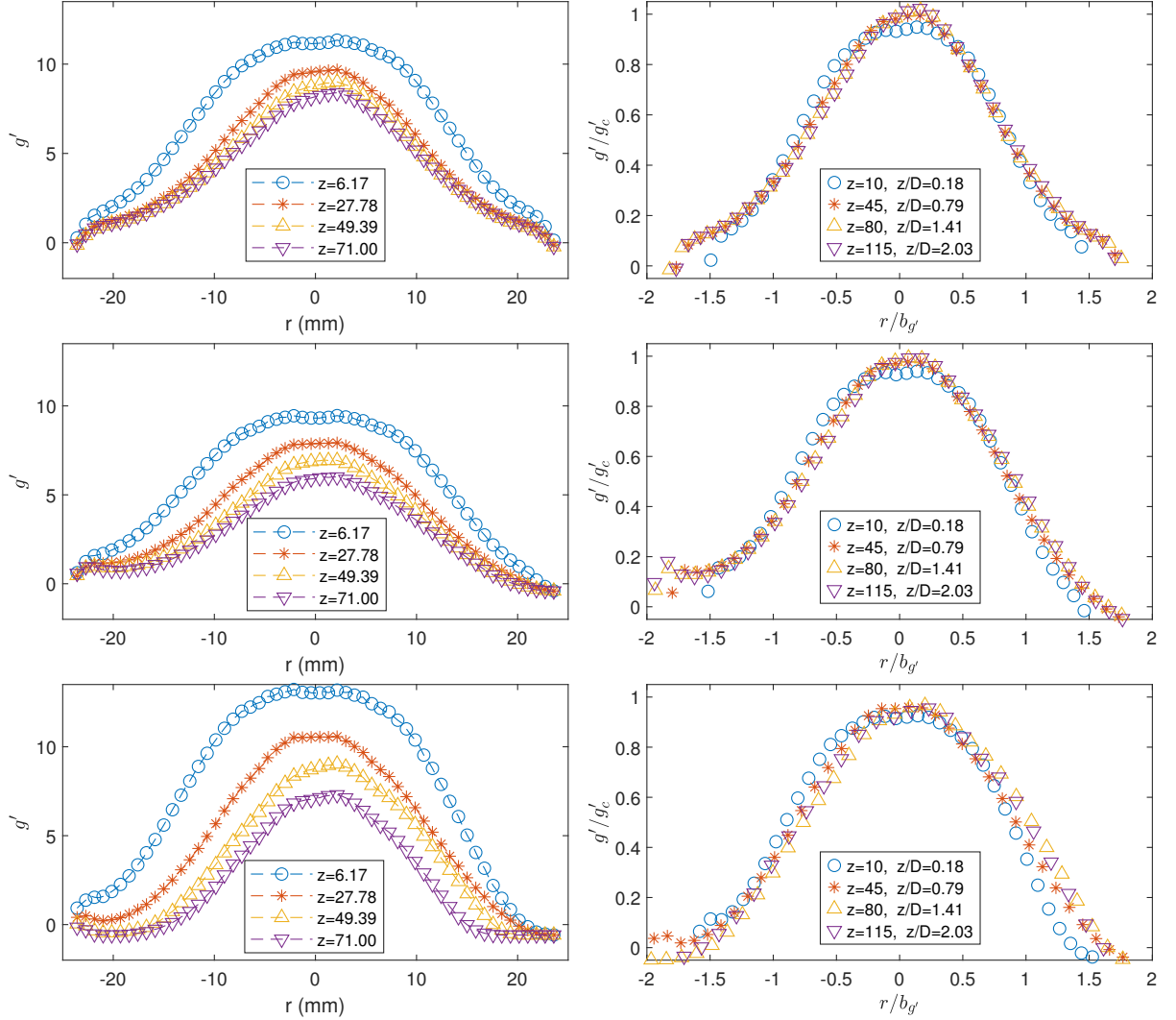


**Fig. 14:** Reduced gravity profiles extracted at different  $z$  planes (left column) and their collapse due to non-dimensionalization with  $g'_c$  and  $b_{g'}$  (right column) for releases -I (top row), II (middle row), and III (bottom row).

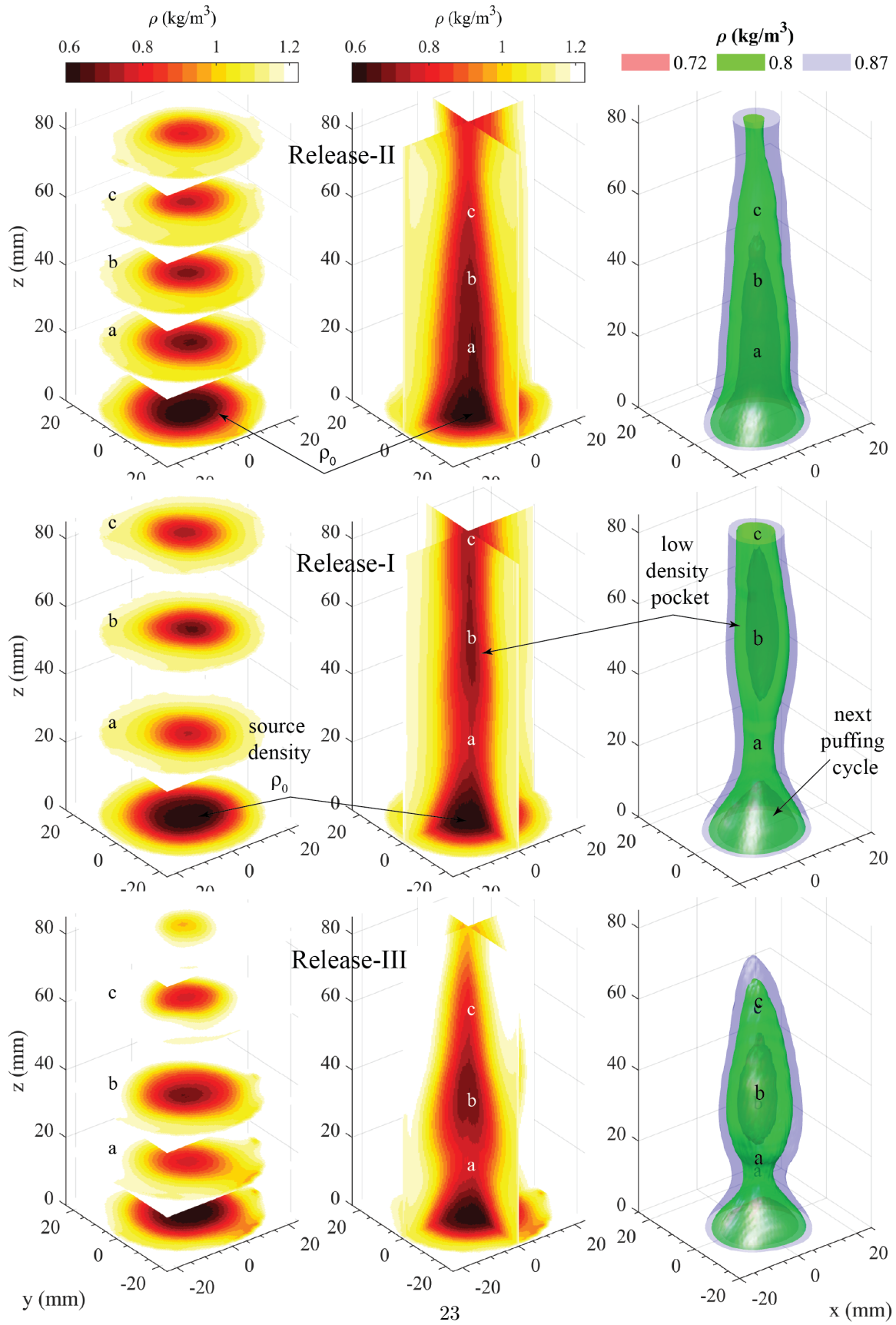


**Fig. 15:** Volumetric visualization of the 3D density field at selected time instances for three release cases. The top row shows the slightly forced plume (Release-II), where no Low Density Pocket (LDP) is observed. The middle and bottom rows show Release-I and Release-III, respectively, highlighting the puffing phenomenon with detached LDPs. Each row includes density slices in transverse (left column) and longitudinal (middle column) planes and iso-surfaces (right column) of density.



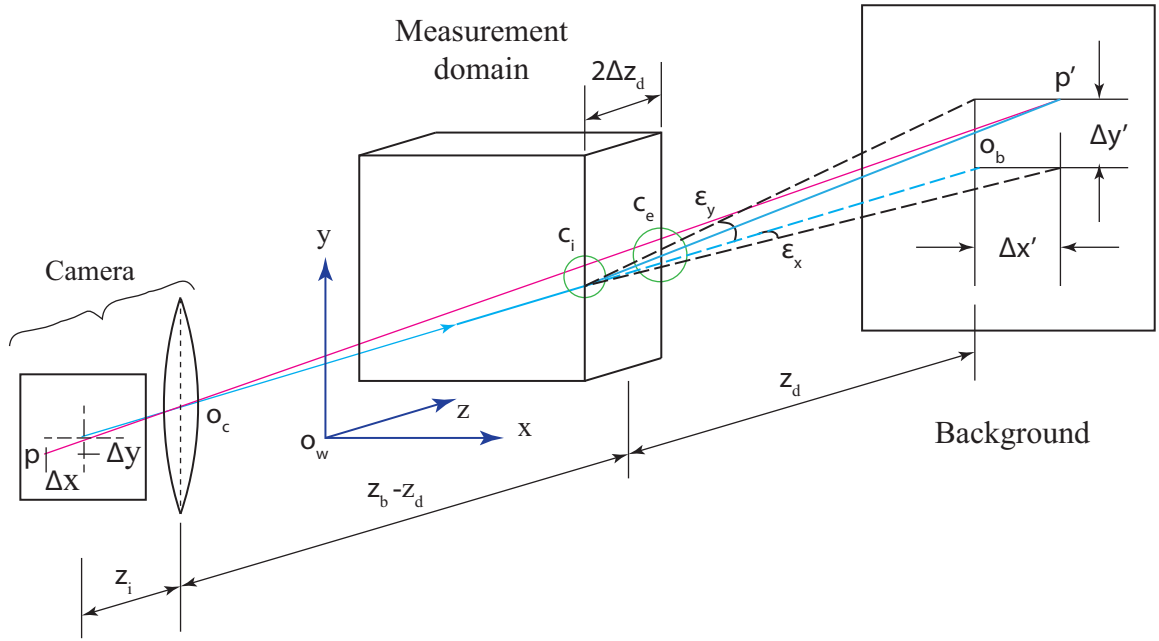


**Fig. A1:** Schematic of the optical setup for background-oriented schlieren